Materials Advances

ROYAL SOCIETY OF CHEMISTRY

PAPER

View Article Online
View Journal | View Issue

Cite this: *Mater. Adv.*, 2025, 6, 3095

Dual-state emission triphenylamine-coumarin fluorescent polymorphs: halochromic reversible fluorescence switching and π–π stacking facilitated picric acid sensing†

Sasikala Ravi,[a] Subramanian Karthikeyan,[b] Mehboobali Pannipara,[c] Abdullah G. Al-Sehemi,[de] Dohyun Moon *[f] and Savarimuthu Philip Anthony *[a]

Organic fluorescence molecules with external stimuli-responsive properties have received significant interest because of their potentiality in various device applications ranging from optoelectronics to biological sciences. Herein, we designed and synthesized dual-state emission (DSE), triphenylamine (TPA)-integrated, coumarin-based donor–acceptor multifunctional fluorophores (**DP2C** and **DP4C**) with an acid responsive pyridine unit. **DP2C** produced fluorescent polymorphs (yellow (**DP2C-Y**) and orange (**DP2C-O**)) and showed tunable solid-state fluorescence (λ_{max} = 537 and 560 nm). **DP2C-O** exhibited relatively strong fluorescence (quantum yield (ϕ_f) = 20%) compared with **DP2C-Y** (ϕ_f = 12%) and **DP4C** (ϕ_f = 16%), which could be attributed to the higher molecular twist in the solid state without any close π-stacking. Both **DP2C** and **DP4C** showed strong fluorescence in the solution state, especially in non-polar toluene and $CHCl_3$ (ϕ_f = 0.69) compared with a 0.5 M quinine sulphate standard in H_2SO_4. Acid responsive pyridine and DSE were utilized to demonstrate reversible fluorescence switching *via* protonation and deprotonation upon exposure to trifluoroacetic acid (TFA) and triethylamine/ammonia (NEt_3)/NH_3 in $CHCl_3$ and solids. TFA addition red shifted the fluorescence with a strong reduction in fluorescence intensity, which was reversed to the initial state by adding NEt_3. Furthermore, **DP2C** and **DP4C** exhibited highly selective fluorescence sensing of picric acid (PA). Limit of detection (LOD) studies for PA sensing indicated sensing values of up to 280.7 and 310 nM corresponding to **DP2C** and **DP4C**, respectively. Single crystal analysis revealed π-stacked arrangements between **DP2C** and PA. Computational studies showed intermolecular charge transfer from **DP2C** to the PA unit in the lowest unoccupied molecular orbital (LUMO), supporting fluorescence quenching. Fluorescent PMMA and PVA polymer thin films were fabricated and demonstrated reversible fluorescence switching and PA sensing, respectively, in thin films, indicating the practical utility of the developed DSE fluorophores.

Received 21st January 2025,
Accepted 21st March 2025

DOI: 10.1039/d5ma00054h

rsc.li/materials-advances

Introduction

Functional organic fluorescence molecules are important candidates for many applications, including organic light-emitting diodes (OLEDs), displays, sensors and bioimaging.[1–10] Particularly, dual-state emission (solution- and solid-state) molecules with stimuli-responsive properties have received significant attention in recent years since they can be utilized in their molecular and aggregated states for improving device performance and fabrication.[11–13] For instance, strong fluorescence in a de-aggregated state allows the fabrication of fluorescent polymer composite thin films for re-usable sensors, data storage and anticounterfeiting applications.[14–17] In general, organic π-conjugated planar molecules show strong emission in solution but weak or no emission in the condensed state owing to the aggregation-caused quenching (ACQ) effect.[18,19]

[a] *School of Chemical & Biotechnology, SASTRA Deemed University, Thanjavur- 613401, Tamil Nadu, India. E-mail: philip@biotech.sastra.edu*
[b] *PG and Research Department of Chemistry, KhadirMohideen College (affiliated to Bharathidasan University), Adirampattinam, Tamil Nadu, India*
[c] *Central Labs, King Khalid University, AlQuráa, Abha, Saudi Arabia*
[d] *Research center for Advanced Materials Science, King Khalid University, Abha 61413, Saudi Arabia*
[e] *Department of chemistry, King Khalid University, Abha 61413, Saudi Arabia*
[f] *Beamline Department, Pohang Accelerator Laboratory, 80 Jigokro-127 beongil, Nam-gu, Pohang, Gyeongbuk, Korea. E-mail: dmoon@postech.ac.kr*

† Electronic supplementary information (ESI) available: NMR and crystal data and structure, photophysical studies. CCDC 2415627–2415630. For ESI and crystallographic data in CIF or other electronic format see DOI: https://doi.org/10.1039/d5ma00054h

In contrast, generating fluorophores with a non-planar core unit produces aggregation-induced emission (AIE) and exhibits weak emission in solution due to the molecular flexibility and free rotation of single bonds.[20–22] Hence, DSE fluorophores is relatively challenging than designing solution or solid-state emissive molecules and requires a special design strategy.[23–25] In general, organic π-conjugated fluorophores with donor–acceptor units connected through an aliphatic linker mostly exhibit strong solid-state fluorescence.[26] However, donor–acceptor units interconnected through an aromatic linker in a π-conjugated structure leads to DSE due to the restriction of structural flexibility.[27,28] Integrating imidazole and triazole acceptor units results in strongly enhanced fluorescence in the solution and solid states, along with improved stability.[29–32] Excited-state intramolecular proton transfer (ESIPT) molecules with a strong intramolecular H-bonding functionality exhibited DSE and stimuli-induced fluorescence switching.[33–35] Introducing aliphatic chains or bulky groups into aromatic fluorophores, such as pyrene, perylene diimide and BODIPY, isolates the fluorophores, preventing π-stacking and leading to enhanced fluorescence in the solution and solid states.[36–38] Nevertheless, the advantages of DSE fluorophores for demonstrating multifunctional applications are rarely reported. The present work aims to develop DSE molecules with functional units to achieve stimuli-responsive fluorescence switching and sensing in the solution and solid states.

Triphenylamine (TPA), a propeller-shaped non-planar unit, has been extensively utilized for synthesising donor–acceptor fluorophores with tunable and switchable emission.[39–41] Its non-planar conformation hinders close π-stacking between molecules in the solid state, producing AIEgens with strong fluorescence.[42,43] Its structural tailorability allows modulation of π-conjugation and lead to fluorescence tuning from blue to NIR light.[44–46] Similarly, heteroaromatic π-conjugated coumarin derivatives have been employed for developing fluorescence chemosensors and room temperature phosphorescent molecules.[47–52] The bio-compatibility and structural flexibility of coumarin make it suitable for many biological applications, including bioimaging as well as synthesis of antibiotics and anticoagulants.[53–55] Coumarin functionality has also been exploited for synthesizing ESIPT molecules with significantly red-shifted fluorescence.[56] Therefore, the integration of planar heteroaromatic coumarin with non-planar TPA is expected to produce a DSE molecule with functional properties. In this study, we synthesized TPA-based pyridine isomers with coumarin units (**DP2C** and **DP4C**), which exhibited DSE, polymorphism, switchable fluorescence and picric acid (PA) sensing (Scheme 1). **DP2C** produced yellow (**DP2C-Y**) and orange (**DP2C-O**) emitting fluorescent polymorphs. **DP4C** displayed yellow fluorescence in the solid state. **DP2C-Y** exhibited a relatively lower conformational twist between coumarin and pyridine compared with **DP2C-O**. **DP4C** showed a nearly coplanar conformation with slipped π-stacking. Both isomers demonstrated strong fluorescence in non-polar solvents, such as toluene, $CHCl_3$ and EtOAc. The fluorescence was significantly enhanced (2.5 times) for both isomers upon integration into a PMMA polymer matrix owing to structural rigidification and a hydrophobic environment.

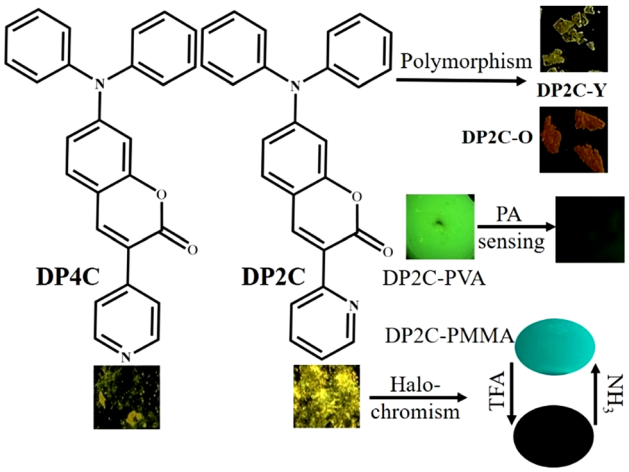

Scheme 1 Molecular structures of **DP2C** and **DP4C**, images of fluorescent polymorphs of **DP2C**, digital fluorescence images, stimuli-responsive fluorescence switching and PA sensing.

The presence of an acid-responsive pyridine unit was utilized to demonstrate acid/base-dependent fluorescence switching in solution, solid state, and the PMMA polymer matrix. **DP2C** and **DP4C** exhibited highly selective fluorescence quenching for PA in solution and the PVA polymer matrix. Single crystal analysis suggested the formation of a supramolecular complex with PA. Computational studies revealed intermolecular charge transfer from **DP2C** to PA in LUMO, which contributed to fluorescence quenching.

Experimental

Diphenylamine, 3-iodoanisole, phosphorus oxychloride, boron tribromide, piperidine, 2-/3-pyridyl acetonitrile, potassium carbonate and solvents were procured from Merck.

Synthesis of 4-(diphenylamino)-2-hydroxybenzaldehyde

4-(Diphenylamino)-2-hydroxybenzaldehyde was synthesized according to previous reports.[57,58]

Synthesis of coumarin integrated TPA pyridine isomers (Scheme S1, ESI†)

Aldehyde (0.25 g, 1 mmol), 2/4-pyridylacetonitrile (0.18 g, 1.8 mmol) and piperidine (0.07 g, 1 mmol) were mixed and refluxed for 12 h. After completion of the reaction, the mixture was extracted, concentrated and purified through column chromatography using ethyl acetate: hexane (15 : 85) mixture as the eluent.

7-(Diphenylamino)-3-(pyridin-2-yl)-2*H*-chromen-2-one

(DP2C): M.pt: 180 °C; yield: 81%. ^{1}H NMR (600 MHz, $CDCl_3$) δ 8.68 (s, 1H), 8.59 (d, 1H), 8.37–8.36 (d, J = 6 Hz, 1H), 7.74–7.71 (t, J = 9 Hz, 1H), 7.35–7.34 (d, J = 6 Hz, 1H), 7.30–7.27 (m, 4H), 7.22–7.20 (m, 1H), 7.14–7.11 (m, 6H), 6.83–6.81 (dd, J = 9 Hz, 1H), 6.77–6.76 (d, J = 6 Hz, 1H) ppm. ^{13}C NMR (150 MHz, $CDCl_3$) δ 160.6, 155.7, 152.3, 151.5, 148.2, 145.8, 143.1, 129.8,

129. 7, 126.4, 125.5, 124.0, 122.8, 116.6, 112.8, 106.7, 105.5 ppm. HRMS (*m*/*z*) $C_{26}H_{18}N_2O_2$ calculated: 390.1368; found: 389.9920.

7-(Diphenylamino)-3-(pyridin-2-yl)-2*H*-chromen-2-one (DP4C): M.pt: 190 °C, yield: 76%. ^{1}H NMR (600 MHz, $CDCl_3$) δ 8.58 (s, 1H), 7.80 (s, 1H), 7.60–7.59 (d, J = 6 Hz, 2H), 7.31–7.25 (m, 6H), 7.14–7.12 (m, 6H), 6.84–6.82 (dd, J = 9 Hz, 1H), 6.77–6.76 (d, J = 6 Hz, 1H) ppm. ^{13}C NMR (150 MHz, $CDCl_3$) δ 160.1, 155.5, 152.2, 149.9, 145.7, 142.9, 141.4, 130.1, 129.8, 128.9, 126.4, 125.5, 122.5, 116.5, 112.4, 105.7 ppm. HRMS (*m*/*z*) $C_{26}H_{18}N_2O_2$ calculated: 390.1368; found: 390.0590.

Characterization

NMR spectra were measured on JEOL 600 MHz. Absorption and fluorescence spectra were recorded using a Jasco V-730ST UV-visible spectrophotometer and a FP-8300 spectrofluorometer. Absolute quantum yields for solids were measured using an integrating sphere attached to the FP-8300 spectrofluorometer. Single crystals were coated with paratone-N oil, and the diffraction data were measured using synchrotron radiation (λ = 0.62998 Å) on an ADSC Quantum-210 detector at 2D SMC with a silicon (111) double crystal monochromator (DCM) at the Pohang Accelerator Laboratory, Korea. CCDC no. 2415627–2415630 contain the supplementary crystallographic data for this study. The HOMO, LUMO and band gap of **DP2C**/**DP4C** isomers were studied in the gas phase using the B3PW91/6-31+G(d,p) level of theory (Gaussian 09 package). The molecular structures for the calculations were obtained from the single crystal data and used without structural optimization.

Results and discussion

TPA-based coumarin pyridine isomers, **DP2C** and **DP4C**, were synthesized *via* intramolecular cyclisation, as presented in Scheme 2. The 4-(diphenylamino)-2-hydroxybenzaldehyde precursor was synthesized as per the procedure depicted in Scheme S1 (ESI†). The coupling reaction between 4-(diphenylamino)-2-hydroxybenzaldehyde and pyridine acetonitrile in ethanol in the presence of piperidine base produced **DP2C** and **DP4C**, respectively, in good yield. The structures of both isomers were confirmed using NMR and mass spectrometry (ESI†).

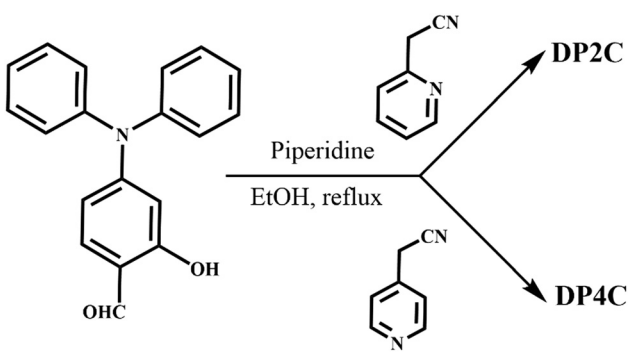

Scheme 2 Synthetic scheme for **DP2C** and **DP4C**.

Single crystals of **DP2C** and **DP4C** were grown through the slow evaporation method to confirm the structure and analyse the molecular assembly in the solid state (Tables S1–S3, ESI†). **DP2C** produced yellow and orange-emitting polymorphic crystals (**DP2C-Y** from $CHCl_3$–MeOH and **DP2C-O** from MeOH) depending on the solvent of crystallization. **DP4C** did not exhibit polymorphism and formed yellow fluorescent crystals. PXRD of **DP2C-Y** and **DP2C-O** showed different patterns, confirming polymorphism (Fig. S1, ESI†). The polymorphs (**DP2C-Y** and **DP2C-O**) and pyridine isomer (**DP4C**) displayed different molecular twists between the coumarin and pyridine units in the solid state (Fig. 1a). The conformational twist was analysed using the torsional (τ) angle between pyridine and coumarin (Table 1). The comparison of torsion angles suggested higher molecular twist in **DP2C-O** compared with that in **DP2C-Y** and **DP4C**. A coplanar conformation with the lowest molecular twist was observed in **DP4C**. This variation in the conformational twist resulted in different molecular assemblies and intermolecular interactions in the crystal lattice of **DP2C-Y** and **DP2C-O**. The intermolecular H-bonding between the carbonyl oxygen and TPA phenyl hydrogen produced a dimer with an opposite molecular arrangement (Fig. 1b). The slipped π-interactions

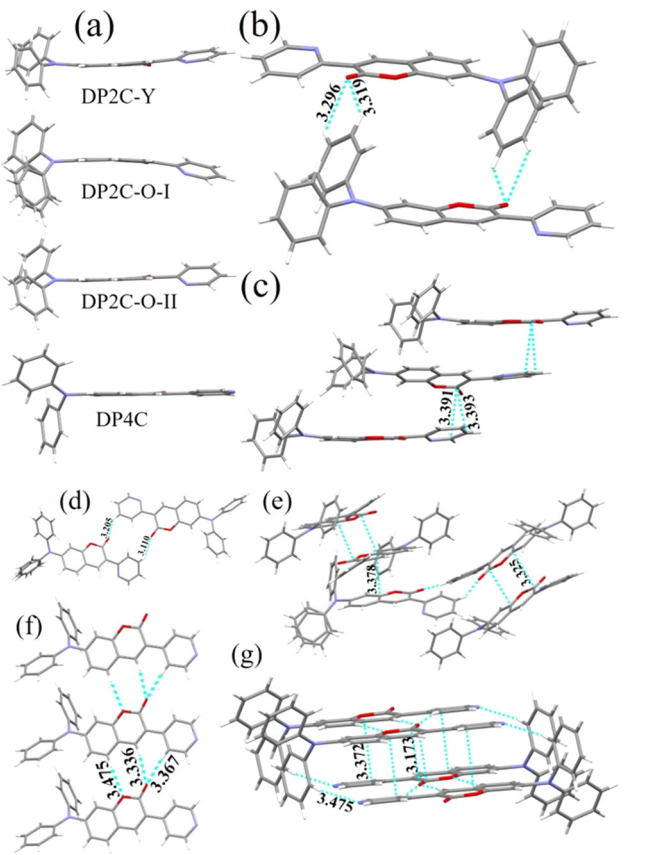

Fig. 1 (a) Molecular structure in the crystal lattice of **DP2C-Y**, **DP2C-O** and **DP4C**, and intermolecular interactions in the crystal lattice of (b) and (c) **DP2C-Y**, (d) and (e) **DP2C-O** and (f) and (g) **DP4C** [C (grey), H (white), N (blue) and O (red)]. Dotted lines indicate hydrogen bonding, C–H···π and π···π interactions in Å.

Table 1 Torsion angle (τ) of **DP2C** and **DP4C** in the crystal lattice

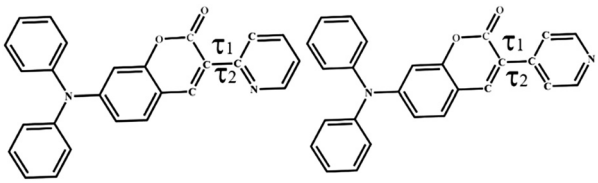

	Torsion angle (τ)	
	τ_1	τ_2
DP2C-Y	17.06	13.54
DP2C-O	21.05 (I)	17.61 (I)
	26.16 (II)	23.46 (II)
DP4C	6.14	4.86

between pyridine and coumarin carbonyl carbon produced a layered structure with a parallel arrangement (Fig. 1c). Two molecules were present in the asymmetric unit of **DP2C-O**, and one of the TPA phenyl units showed disorder (Fig. S2, ESI†). The complimentary H-bonding between carbonyl oxygen and phenyl hydrogen connected both the molecules and produced an oppositely arranged dimer (Fig. 1d). Furthermore, each molecule of the dimer formed C–H$\cdots\pi$ and slipped $\pi\cdots\pi$ interactions and a network structure in the crystal lattice (Fig. 1e). **DP4C** exhibited a nearly coplanar conformation between coumarin and pyridine (Fig. 1a). The intermolecular H-bonding between coumarin oxygen and phenyl hydrogen produced a sheet structure with a parallel arrangement of molecules in the crystal lattice (Fig. 1f). The sheets were interconnected through $\pi\cdots\pi$ interactions and H-bonding, resulting in an oppositely arranged structure (Fig. 1g). The molecular conformational twist differences in **DP2C** polymorphs and **DP4C** caused distinct molecular packing in the crystal lattice (Fig. S3, ESI†).

The donor–acceptor structure with non-planar molecular confirmation was expected to produce solid-state fluorescence. **DP2C-Y** showed dual emission in the solid state at 498 and 537 nm, whereas **DP2C-O** showed strong fluorescence at 560 nm (Fig. 2a). **DP4C** exhibited yellow fluorescence at 546 nm. Absolute quantum yield measurement revealed the highest efficiency for **DP2C-O** (20%), which could be attributed to the more twisted molecular conformation (Table 1). **DP2C-Y** and **DP4C** showed slightly lower fluorescence efficiencies of 12% and 16%, respectively.

In solution, the absorption of **DP2C** and **DP4C** did not show a significant change with solvent polarity, suggesting a non-polar ground state (Fig. S4, ESI†). Both molecules exhibited an intramolecular charge transfer (ICT) peak between 405 and 410 nm in polar to non-polar solvents. In contrast, **DP2C** and **DP4C** showed solvent polarity-dependent tunable fluorescence (Fig. 2b and c, Table 2). **DP2C** and **DP4C** displayed dual emission peaks: a locally excited (LE) state (shorter wavelength) and a charge transfer (CT) state emission (longer wavelength), with varied peak intensity depending on solvent polarity. In toluene, LE state shorter emission (λ_{max} = 481 (**DP2C**) and 491 nm (**DP4C**)) was more intense compared with CT state emission (λ_{max} = 532 nm). However, CT state emission became stronger in $CHCl_3$, THF and EtOAc.

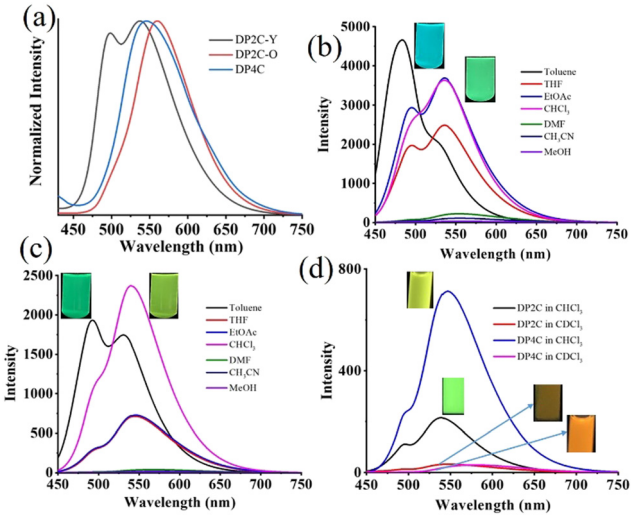

Fig. 2 (a) Solid-state fluorescence, solvent polarity dependent fluorescence tuning of (b) **DP2C** and (c) **DP4C** and (d) fluorescence of **DP2C/DP4C** in $CHCl_3$ and $CDCl_3$. Digital fluorescence images are integrated into the corresponding spectra. λ_{exc} = 420 nm (for spectra) and 365 nm (for images).

Table 2 Quantum yield of **DP2C** and **DP4C** in solution, solids and polymer (PMMA) matrix

	DP2C		**DP4C**	
	λ_{max} (nm)	ϕ_f	λ_{max} (nm)	ϕ_f
Solvent[a]				
Toluene	483, 530	0.41	491, 532	0.37
THF	495, 536	0.45	493, 545	0.13
EtOAC	494, 536	0.66	493, 545	0.12
$CHCl_3$	494, 536	0.69	494, 540	0.47
DMF	492, 553	0.04	488, 564	—
CH_3CN	492, 553	0.03	490, 569	—
CH_3OH	492, 548	—	488, 567	—
Solids[b]				
DP2C-Y	497, 537	12%		
DP2C-O	560	20%		
DP4C	547	16%		
Polymer matrix[b]				
DP2C-PMMA	481, 528	55.2%		
DP4C-PMMA	492, 526	63.3%		

[a] Quantum yields were measured by comparing with standard quinine (0.5 M H_2SO_4). [b] Absolute quantum yields.

The fluorescence was very weak in polar protic/aprotic solvents with a further red shift in longer wavelength emission. This insignificant change in absorption and tunable fluorescence with solvent polarity indicated the formation of twisted intramolecular charge transfer (TICT).[59] The red shift in emission with efficiency reduction in polar solvents is characteristic of the TICT state.[60] Thus, **DP2C** and **DP4C** exhibited strong LE state emission in non-polar toluene, whereas strong TICT emission in $CHCl_3$ and THF. Excitation spectra of **DP2C**/**DP4C** in toluene revealed similar spectra except for an increase in intensity for LE state emission compared with CT state emission (Fig. S5, ESI†). Excited state lifetime analysis was performed to understand the LE and CT state emission of **DP2C**

and **DP4C** (Fig. S6 and Table S4, ESI†). Toluene was chosen as a representative solvent. Both **DP2C** and **DP4C** revealed biexponential decay components with nanosecond lifetimes (Table S4, ESI†). Blue-shifted emission showed a shorter lifetime compared with red-shifted emission in both compounds (Fig. S6a, ESI†). This shorter and longer lifetime of blue and red-shifted emissions could be attributed to the LE and CT states, respectively. Moreover, biexponential decay with a shorter lifetime for blue-shifted emission was observed in the solid state (Fig. S6b and Table S4, ESI†).

DP2C and **DP4C** displayed unexpected behavior when dissolved in $CDCl_3$. Both compounds showed a significant red shift in the ICT peak and strong quenching of fluorescence in $CDCl_3$ compared with that in $CHCl_3$ (Fig. 2d and Fig. S7, ESI†). The peaks at 418 and 410 nm were red shifted to 467 and 473 nm for **DP2C** and **DP4C**, respectively (Fig. S7, ESI†). Fluorescence also red-shifted for both molecules with strong reduction in intensity (Fig. 2d). This unusual behavior was observed while recording NMR spectra in $CDCl_3$. This unusual absorption and fluorescence modulation in $CDCl_3$ could be attributed to the solute–solvent interaction of $CHCl_3$ present in the solvent in trace amounts. NMR spectra of **DP2C**/**DP4C** showed a $CHCl_3$ peak at 7.19 ppm compared with the usual 7.26 ppm, further supporting the solvent–solute interaction with the pyridine nitrogen.[61] To gain insight into ICT, density functional theory (DFT) calculations were performed for **DP2C**/**DP4C**. Electron density was mostly occupied in the triphenylamine unit in HOMOs but shifted to the coumarin unit in LUMOs in all three structures (Fig. 3). The comparison of the optical band gap suggested a lower band gap for **DP2C-O** (3.47 eV) compared with that for **DP2C-Y** (3.58 eV), supporting fluorescence tuning through polymorphism.

The strong dual-state fluorescence and acid-responsive pyridine functionality of **DP2C** and **DP4C** provided an excellent opportunity for achieving halochromic fluorescence switching through protonation and deprotonation. **DP2C** powder showed strong fluorescence at 550 nm, which was red-shifted to 635 nm with strong quenching upon exposure to TFA (Fig. 4a).

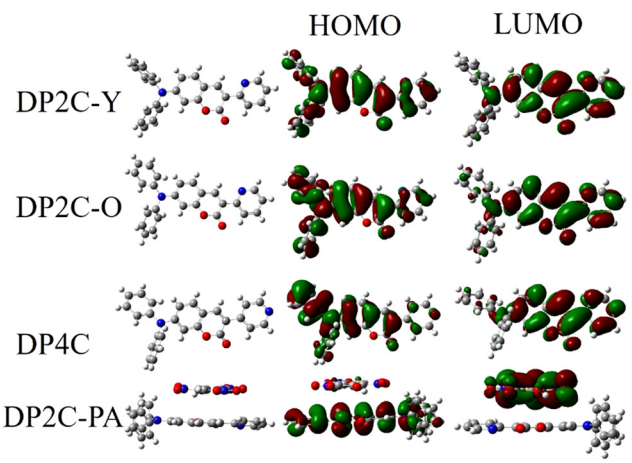

Fig. 3 HOMO–LUMO diagram for **DP2C-Y**, **DP2C-O**, **DP4C** and **DP2C** with PA.

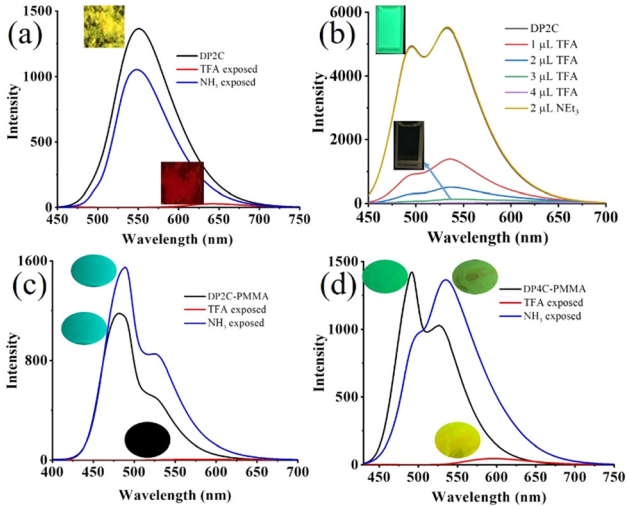

Fig. 4 Acid (TFA)–base (NEt_3/NH_3) exposure-dependent fluorescence switching of (a)–(c) **DP2C** and (d) **DP4C**. (a) Solid-state, (b) $CHCl_3$ and (c, d) PMMA matrix. Digital fluorescence images are integrated into the corresponding spectra. λ_{exc} = 420 nm (for spectra) and 365 nm (for images).

The protonation of nitrogen could increase the electron-withdrawing character and red-shift the emission. To confirm the protonation of pyridine, NMR was recorded in the presence of TFA. The addition of 1 eq. TFA to **DP2C** in $CDCl_3$ showed a downfield shift of NMR signals (Fig. S8, ESI†). Additionally, a new peak appeared at δ 9.5 ppm, corresponding to the Py-NH^+ proton, confirming pyridine nitrogen protonation. Fluorescence was completely reversed to the initial state upon NH_3 exposure. The strong fluorescence of **DP4C** powder was red-shifted from 557 to 632 nm upon TFA exposure (Fig. S9, ESI†). Unlike the NH_3 exposure in **DP2C**, that in **DP4C** did not show complete reversal of fluorescence and reversed only up to 593 nm. Furthermore, protonated **DP4C** showed relatively higher fluorescence intensity compared with **DP2C** after TFA exposure. In $CHCl_3$, **DP2C** showed π–π* and ICT absorption at 340 and 409 nm, respectively (Fig. S10a, ESI†). TFA addition red-shifted ICT absorption to 502 nm, while the intensity of π–π* absorption increased without changing the peak position. The red-shifted absorption was reversed to the initial state upon NEt_3 addition (Fig. S10b, ESI†). **DP4C** in $CHCl_3$ was more sensitive to TFA and NEt_3 (Fig. S10c and d, ESI†). The absorption immediately changed from 413 to 495 nm upon the addition of 1 μL of TFA but gradually reversed with the addition of NEt_3. **DP2C** showed dual emission at 494 and 536 nm in $CHCl_3$ (Fig. 4b). The fluorescence was completely quenched upon the addition of TFA and reversed to the initial state upon the addition of NEt_3. **DP4C** in $CHCl_3$ also exhibited similar off–on fluorescence switching upon the addition of TFA and NEt_3 (Fig. S11, ESI†).

The **DP2C** and **DP4C** fluorophores were integrated into a PMMA polymer matrix to demonstrate reversible fluorescence switching in a thin film. **DP2C**/**DP4C** (25 μL of 10^{-3} M) was added to PMMA (1 wt%) toluene solution and stirred at 70 °C temperature for 30 min. Thin films of PMMA-**DP2C**/**DP4C** were fabricated using the drop casting method. Interestingly,

integrating the fluorophore into the PMMA matrix significantly enhanced its fluorescence efficiency (Table 2). **DP2C**-PMMA and **DP4C**-PMMA thin films showed fluorescence efficiencies of 55.2% and 63.3%, respectively (Fig. 4c and d). The enhancement of fluorescence efficiency was attributed to the rigidification of the molecular structure under a hydrophobic environment. In the PMMA matrix, LE state emission (481 nm) became stronger than CT state emission (528 nm, Fig. 4c). FTIR spectra indicated an increase in the C=O wavenumber after integrating **DP2C**/**DP4C** fluorophores with the PMMA matrix (Fig. S12 and S13, ESI†). PMMA carbonyl stretching appeared at 1731 cm^{-1}. **DP2C** and **DP4C** carbonyl stretching increased from 1720 and 1699 to 1734 and 1743, respectively. This suggested the interaction between the fluorophore and the PMMA matrix, which might have contributed to the rigidification of the fluorophore. The fluorescence was completely quenched upon TFA exposure and reversed to the initial state upon NH_3 exposure. Digital fluorescence images also confirmed reversible fluorescence switching due to TFA/NH_3 exposure. The off–on fluorescence switching by TFA/NEt_3, could be achieved for several cycles without significant changes in the fluorescence intensity or peak position (Fig. S14, ESI†). The **DP4C**-PMMA thin film also showed strong LE state emission (492 nm) than CT state emission (526 nm, Fig. 4d). TFA exposure red-shifted the fluorescence (583 nm) with a strong reduction in intensity. The fluorescence intensity was reversed upon NH_3 exposure, but CT emission (536 nm) appeared stronger than LE state emission after NH_3 exposure. Both thin films showed slight self-recovery of fluorescence in 24 h (Fig. S15a and b, ESI†). Absorption spectra of PMMA-**DP2C**/**DP4C** fluorophore thin films showed a strong ICT peak around 410 nm, which was red-shifted upon TFA exposure and reversed to the initial state upon NH_3 exposure (Fig. S15c and d, ESI†).

Dual state emission of **DP2C** and **DP4C** was further explored for nitroaromatic compound (NACs) sensing because of their intermolecular interacting functionality and planar coumarin π-conjugated ring. NACs were dissolved in $CHCl_3$ (10^{-3} M) and added to a $CHCl_3$ solution of **DP2C**/**DP4C** (10^{-4} M). The fluorescence of **DP2C**/**DP4C** was selectively quenched by PA, while the addition of other NACs did not significantly alter the fluorescence (Fig. 5a and b). Digital fluorescence images also showed the complete disappearance of green fluorescence after the addition of PA. Concentration-dependent studies showed a gradual decrease in fluorescence intensity with increasing PA concentration (Fig. 5c and Fig. S16a, ESI†). The LOD obtained from concentration-dependent studies on **DP2C**/**DP4C** with PA indicated a sensing value of up to 280.7/310 nM (Fig. S16b and c, ESI†). Furthermore, absorption spectra of **DP2C**/**DP4C** probes with NACs showed a selective response to PA (Fig. S17, ESI†). **DP2C** with PA showed appearance of a new peak at 340 nm and a reduction of the ICT peak at 409 nm (Fig. S17a, ESI†). 4-Nitroaniline (4-NA) exhibited a change in absorption, whereas other NACs did not show any significant change. **DP4C** showed a more sensitive response, with a new red-shifted CT peak at 482 nm and a new peak at 340 nm (Fig. S17b, ESI†). PA concentration-dependent absorption studies revealed a gradual increase in peak intensity at 340 nm and an extension of $\lambda_{cut\text{-}off}$ beyond 475 nm for **DP2C** (Fig. S17c, ESI†). **DP4C** exhibited a gradual disappearance of the ICT peak at 410 nm and the emergence of a new red-shifted peak at 482 nm and 340 nm (Fig. S17d, ESI†). The absorption and fluorescence studies indicated a selective interaction between **DP2C**/**DP4C** and PA. **DP2C**/**DP4C** could interact with PA *via* (i) protonation of pyridine nitrogen and (ii) intermolecular H-bonding/π···π interactions.

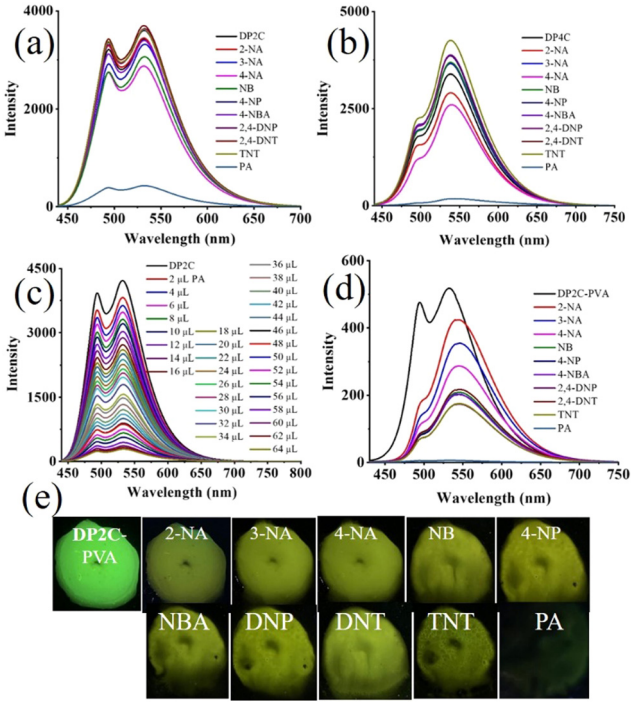

Fig. 5 Fluorescence sensing of PA (10^{-4} M) using (a) **DP2C** (10^{-5} M) and (b) **DP4C** (10^{-5} M), (c) PA concentration-dependent fluorescence change of **DP4C** in $CHCl_3$, (d) fluorescence sensing of PA in an aqueous medium using the **DP2C**-PVA thin film and (e) digital fluorescence images of **DP2C**-PVA after dipping in aqueous solution of NACs. λ_{exc} = 420 nm (for spectra) and 365 nm (for images).

To understand the mechanism of **DP2C**/**DP4C** selective fluorescence quenching by PA, single crystals were attempted to be grown along with PA from a $CHCl_3$–methanol mixture *via* slow evaporation of the solvent. **DP2C** produced quality dark-red single crystals with PA (Fig. 6a). In contrast, **DP2C** crystals without PA appeared pale yellow. The crystal lattice of **DP2C-PA** comprised two **DP2C** molecules and one PA, along with a solvent methanol molecules (Fig. 6a and Table S5, ESI†). Oxygen in one of the nitro groups showed disorder in the crystal lattice. The PA hydroxy group either underwent deprotonation or participated in intermolecular H-bonding. The methanol solvent formed intermolecular H-bonding with **DP2C** carbonyl oxygen and the nitro group of PA. Another PA molecule exhibited direct intermolecular interactions with **DP2C** *via* nitro with carbonyl oxygen and pyridine nitrogen. These intermolecular interactions produced a layered structure in the crystal lattice (Fig. 6a). PA further showed strong π···π interactions with coumarin and produced alternative packing

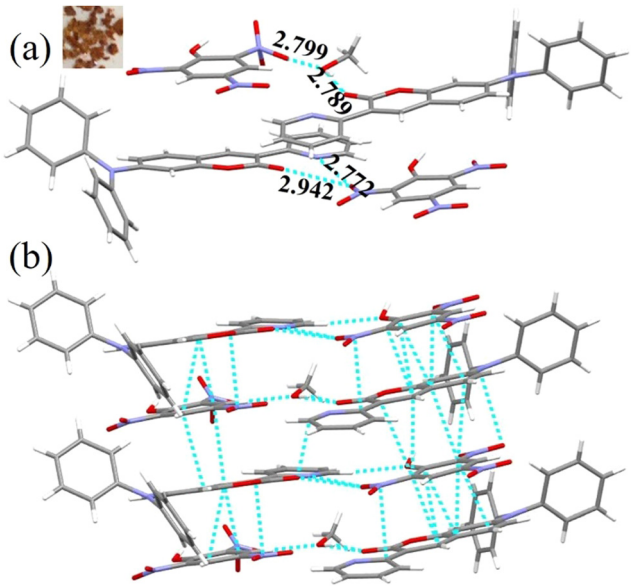

Fig. 6 (a) Molecular structure in the crystal lattice of **DP2C-PA** and (b) π···π stacked arrangements of **DP2C** and PA in the crystal lattice [C (grey), H (white), N (blue) and O (red)]. Dotted lines indicate hydrogen bonding, C–H···π and π···π interactions in Å. The distances between PA and **DP2C** range between 3.030 and 3.396 Å. **DP2C-PA** crystal image is shown in the inset.

of PA and coumarin in the crystal lattice (Fig. 6b). The π···π stacking of PA and coumarin might facilitate charge transfer from coumarin to PA, which could result in fluorescence quenching. Computational studies indicated that electron density was primarily located in the TPA-coumarin unit in HOMO but was completely transferred to PA in LUMO (Fig. 4). Thus, HOMO–LUMO calculations supported the fluorescence quenching by intermolecular charge transfer from **DP2C**/**DP4C** to PA. **DP2C**/**DP4C** showed a red shift of fluorescence with a reduction in intensity upon TFA exposure, further indicating that fluorescence quenching was not due to protonation of pyridine. To improve the practical utility of PA sensing, PVA-**DP2C**/**DP4C** polymer thin films were fabricated and PA sensing was performed in an aqueous medium. PVA (1 wt%) was dissolved in water and 25 μL of **DP2C**/**DP4C** (10^{-3} M in CH_3CN) was introduced. The resulting solution was stirred at room temperature for 1 h to ensure uniform distribution. Thin films were fabricated using the drop casting method. **DP2C**-PVA showed green fluorescence with dual peaks at 495 and 532 nm (Fig. 5d and e). Dipping the film into an aqueous solution of PA (10^{-3} M) resulted in complete quenching of fluorescence. Dipping into other NAC solutions showed yellow-green fluorescence with reduced intensity. LE state emission appeared as a hump, and CT emission was slightly red-shifted to 543 nm, accompanied by a reduction in intensity with some of the NACs. The digital fluorescence image also showed transformation from green to yellow-green (Fig. 5e). It was observed that the as-fabricated thin film of **DP2C**-PVA showed fluorescence color transformation from green to yellow-green when dipped into an aqueous solution without NACs (Fig. S18, ESI†). The fluorescence color was reversed to green upon drying. Hence, fluorescence changes in **DP2C**/**DP4C**-PVA after dipping into aqueous solutions of other NACs might not be due to the influence of NACs but rather due to dipping into water. Only dipping into PA solution caused complete selective quenching of fluorescence. The **DP4C**-PVA thin film also exhibited similar behavior (Fig. S19, ESI†).

Conclusion

In conclusion, dual state emissive TPA-coumarin-based donor–acceptor pyridine isomers (**DP2C** and **DP4C**) were synthesized and demonstrated fluorescence tuning, reversible fluorescence switching and highly selective PA sensing. The **DP2C** and **DP4C** isomers showed strong fluorescence in the solution and solid states. Integration of fluorophores into the PMMA polymer matrix resulted in highly enhanced fluorescence efficiency (up to 2.5–3 times). **DP2C** produced fluorescent polymorphs with yellow (**DP2C-Y**) and orange (**DP2C-O**) emitting crystals, while **DP4C** crystals exhibited only yellow emission. **DP2C-O** displayed relatively higher molecular conformational twist with well-separated packing in the crystal lattice, leading to enhanced solid-state fluorescence efficiency (ϕ_f = 20%). The slipped π-stacked arrangements in **DP2C-Y** and **DP4C** produced slightly lower efficiencies (ϕ_f = 16% and 12%, respectively). Both isomers exhibited strong fluorescence in non-polar solvents. The presence of the acid-responsive pyridine functionality was utilized to achieve reversible off–on fluorescence switching upon acid–base exposure in solution, solids and polymer-fluorophore thin films. Furthermore, the **DP2C** and **DP4C** isomers exhibited highly selective fluorescence sensing of PA in $CHCl_3$, with LODs of up to 280.7 and 310 nM, respectively. Moreover, PVA-fluorophore thin films exhibited highly selective fluorescence quenching upon dipping into an aqueous solution of PA, suggesting potential for PA sensing device fabrication. Single crystal analysis showed the formation of π-stacking arrangements between **DP2C** and PA *via* intermolecular interactions, which facilitated energy transfer from the fluorophore to PA and fluorescence quenching.

Data availability

The data that support the findings of this study are available from the corresponding author upon reasonable request.

Conflicts of interest

There are no conflicts to declare.

Acknowledgements

Financial support from the Science and Engineering Research Board (SERB), CRG/2020/003978, New Delhi, India is acknowledged with gratitude. The Deanship of Research and graduate

studies at King Khalid University is greatly appreciated for funding through large research project (RGP2/397/46).

References

1 H. Liu, Y. Fu, B. Z. Tang and Z. Zhao, *Nat. Commun.*, 2022, **13**, 5154.
2 H. Li, N. Xie, J. Wang, Y. Zhao and B. Liang, *Org. Electron.*, 2021, **88**, 106004.
3 L. Xing, J. Wang, W.-C. Chen, B. Liu, G. Chen, X. Wang, J.-H. Tan, S. S. Chen, J.-X. Chen, S. Ji, Z. Zhao, M.-C. Tang and Y. Huo, *Nat. Commun.*, 2024, **15**, 6175.
4 S. R. Nayak, I. Siddiqui Shahnawaz, J.-H. Jou and S. Vaidyanathan, *ACS Appl. Opt. Mater.*, 2023, **1**, 94–106.
5 S. Zuo, Y. Li, T. Ren and L. Yuan, *Sens. Diagn.*, 2024, **3**, 28–39.
6 Y. T. Nguyen, S. Shin, K. Kwon, N. Kim and S. W. Bae, *J. Chem. Res.*, 2023, **47**, 17475198231168961.
7 M. K. Goshisht, G. K. Patra and N. Tripathi, *Mater. Adv.*, 2022, **3**, 2612–2669.
8 H. Liu, G. Jiang, G. Ke, T. Ren and L. Yuan, *ChemPhotoChem*, 2024, **8**, 202300277.
9 R. Gui and H. Jin, *Talanta*, 2024, **275**, 126171.
10 Y. Li, Y. Liu, Q. Li, X. Zeng, T. Tian, W. Zhou, Y. Cui, X. Wang, X. Cheng, Q. Ding, X. Wang, J. Wu, H. Deng, Y. Li, X. Meng, Z. Deng, X. Hong and Y. Xiao, *Chem. Sci.*, 2020, **11**, 2621–2626.
11 L. A. Rodriguez-Cortes, A. Navarro-Huerta and B. Rodriguez-Molina, *Matter*, 2021, **4**, 2622–2624.
12 G. Xia, L. Si and H. Wang, *Mater. Today Chem.*, 2023, **30**, 101596.
13 N. A. Kukhta and M. R. Bryce, *Mater. Horiz.*, 2021, **8**, 33–55.
14 B. Ma, S. Wu and F. Zeng, *Sens. Actuators, B*, 2010, **145**, 451–456.
15 R. A. Carrillo-Betancourt, A. D. López-Camero and J. Hernández-Cordero, *Polymers*, 2023, **15**, 505.
16 J. Jiang, P. Zhang, L. Liu, Y. Li, Y. Zhang, T. Wu, H. Xie, C. Zhang, J. Cui and J. Chen, *Chem. Eng. J.*, 2021, **425**, 131557.
17 J. C.-M. Lee, J.-W. Li, K.-F. Cheng, J.-X. Chen, Y.-S. Ciou, J.-H. Wang, M.-C. Lu, Y.-F. Chen and C.-W. Chiu, *ACS Appl. Electron. Mater.*, 2024, **6**, 1617–1627.
18 Y. Zhan, Z. Yang, J. Tan, Z. Qiu, Y. Mao, J. He, Q. Yang, S. Ji, N. Cai and Y. Huo, *Dyes Pigm.*, 2020, **173**, 107898.
19 P. Das, A. Kumar, A. Chowdhury and P. S. Mukherjee, *ACS Omega*, 2018, **3**, 13757–13771.
20 M. Bonnot, N. Ibrahim, M. Allain and P. Frère, *Molecules*, 2024, **29**, 3135.
21 L. A. Rodríguez-Cortés, F. J. Hernández, M. Rodríguez, R. A. Toscano, A. Jiménez-Sánchez, R. Crespo-Otero and B. Rodríguez-Molina, *Matter*, 2023, **6**, 1140–1159.
22 G. Yashwantrao, P. Gosavi, V. Naik, M. Debnath, S. Seth, P. Badani, R. Srivastava and S. Saha, *J. Mater. Chem. C*, 2025, **13**, 3955–3968.
23 J. L. Belmonte-Vázquez, Y. A. Amador-Sánchez, L. A. Rodríguez-Cortés and B. Rodríguez-Molina, *Chem. Mater.*, 2021, **33**, 7160–7184.
24 T. Stoerkler, T. Pariat, A. D. Laurent, D. Jacquemin, G. Ulrich and J. Massue, *Molecules*, 2022, **27**, 2443.
25 Q. Pei, Y. Yin, F. Tang and A. Ding, *J. Lumin.*, 2023, **263**, 120021.
26 W. Jiang, G. Zhao, W. Tian and Y. Sun, *Molecules*, 2022, **27**, 8099.
27 K. Panthi, R. M. Adhikari and T. H. Kinstle, *J. Phys. Chem. A*, 2010, **114**, 4542–4549.
28 P. Gayathri, S. B. Subramaniyan, A. Veerappan, M. Pannipara, A. G. Al-Sehemi, D. Moon and S. P. Anthony, *Cryst. Growth Des.*, 2022, **22**, 633–642.
29 S. Ravi, P. R. Nithiasri, S. Karthikeyan, M. Pannipara, A. G. Al-Sehemi, D. Moon and S. P. Anthony, *RSC Adv.*, 2023, **13**, 12476–12482.
30 A. Da Lama, J. P. Sestelo, L. Valencia, D. Esteban-Gómez, L. A. Sarandeses and M. M. Martínez, *Dyes Pigm.*, 2022, **205**, 110539.
31 M. Rajasekar, C. Narendran, J. Mary, M. Sivakumar and M. Selvam, *Results Chem.*, 2024, **7**, 101543.
32 S. K. Pathak, Y. Xiang, M. Huang, T. Huang, X. Cao, H. Liu, G. Xie and C. Yang, *RSC Adv.*, 2020, **10**, 15523–15529.
33 P. Gayathri, S. Ravi, S. Karthikeyan, M. Pannipara, A. G. Al-Sehemi, D. Moon and S. P. Anthony, *J. Mol. Struct.*, 2023, **1284**, 135429.
34 P. Gayathri, S. Ravi, K. Akshaya, S. Karthikeyan, M. Pannipara, A. G. Al-Sehemi, D. Moon and S. P. Anthony, *CrystEngComm*, 2022, **24**, 8126–8133.
35 S. Petdee, C. Chaiwai, W. Benchaphanthawee, P. Nalaoh, N. Kungwan, S. Namuang, T. Sudyoadsuk and V. Promarak, *Dyes Pigm.*, 2021, **193**, 109488.
36 A. K. Tripathi, *Spectrochim. Acta, Part A*, 2020, **228**, 117806.
37 M. Zhu, Y. Zhuo, H. Guo, F. Yang and J. Qiu, *J. Lumin.*, 2018, **194**, 264–270.
38 C. T. Arranja, A. Aguiar, T. Encarnação, S. M. Fonseca, L. L. G. Justino, R. A. E. Castro, A. Benniston, A. Harriman, H. D. Burrows and A. J. F. N. Sobral, *J. Mol. Struct.*, 2017, **1146**, 62–69.
39 P. Gayathri, S. Ravi, S. Karthikeyan, M. Pannipara, A. G. Al-Sehemi, V. Madhu, D. Moon and S. P. Anthony, *J. Lumin.*, 2023, **264**, 120173.
40 P. Gayathri, M. Pannipara, A. G. Al-Sehemi and S. P. Anthony, *New J. Chem.*, 2020, **44**, 8680–8696.
41 J. Issac, S. Ravi, K. Chidambaranathan, S. Karthikeyan, M. Pannipara, A. G. Al-Sehemi, S. P. Anthony and V. Madhu, *Cryst. Growth Des.*, 2024, **24**, 3388–3398.
42 Y. Cao, C. Pan and J. Xu, *Mater. Adv.*, 2024, **5**, 3281–3288.
43 S. Ravi, S. Karthikeyan, M. Pannipara, A. G. Al-Sehemi, D. Moon and S. P. Anthony, *Spectrochim. Acta, Part A*, 2024, **315**, 124303.
44 S. Sambathkumar, S. Priyadharshini, M. Fleisch, D. W. Bahnemann, G. Gnana Kumar, S. Senthilarasu and R. Renganathan, *Mater. Lett.*, 2019, **242**, 28–31.
45 S.-N. Zou, C.-C. Peng, S.-Y. Yang, Y.-K. Qu, Y.-J. Yu, X. Chen, Z.-Q. Jiang and L.-S. Liao, *Org. Lett.*, 2021, **23**, 958–962.
46 J. Zhu, J. Zou, Z. Zhang, J. Zhang, Y. Sun, X. Dong and Q. Zhang, *Mater. Chem. Front.*, 2019, **3**, 1523–1531.

47 R. Dondon, V. P. Khilya, A. D. Roshal and S. Fery-Forgues, *New J. Chem.*, 1999, **23**, 923–927.
48 S.-Y. Park, M. Ebihara, Y. Kubota, K. Funabiki and M. Matsui, *Dyes Pigm.*, 2009, **82**, 258–267.
49 I. Cazin, E. Rossegger, G. Guedes de la Cruz, T. Griesser and S. Schlögl, *Polymers*, 2020, **13**, 56.
50 D. Cui, L. Zhang, J. Zhang, W. Li, J. Chen, Z. Guo, C. Sun, Y. Wang, W. Wang, S. Li, W. Huang, C. Zheng and R. Chen, *Angew. Chem.*, 2024, **63**, 11588.
51 D. Zúñiga-Núñez, F. Mura, N. Mariño-Ocampo, B. Zúñiga, J. Robinson-Duggon, R. A. Zamora, H. Poblete, A. Aspée and D. Fuentealba, *Dyes Pigm.*, 2024, **229**, 112290.
52 D. Cao, Z. Liu, P. Verwilst, S. Koo, P. Jangjili, J. S. Kim and W. Lin, *Chem. Rev.*, 2019, **119**, 10403–10519.
53 X.-Y. Liu, K. Xing, Y. Li, C.-K. Tsung and J. Li, *J. Am. Chem. Soc.*, 2019, **141**, 14807–14813.
54 Y. Chen, B. Yu, Y. Cui, S. Xu and J. Gong, *Chem. Mater.*, 2019, **31**, 1289–1295.
55 M. J. Fasco, E. F. Hildebrandt and J. W. Suttie, *J. Biol. Chem.*, 1982, **257**, 11210–11212.
56 M. Mathivanan, J. G. Malecki and B. Murugesapandian, *Spectrochim. Acta, Part A*, 2025, **326**, 125270.
57 A. Kundu, V. V. Kumar and S. P. Anthony, *Inorg.Chem. Commun.*, 2021, **123**, 108301.
58 P. Gayathri, S. Ravi, S. Karthikeyan, A. Mohitkar, S. Jayanty, M. Pannipara, A. G. Al-Sehemi, D. Moon and S. P. Anthony, *New J. Chem.*, 2023, **47**, 7288–7298.
59 A. M. El-Zohry, E. A. Orabi, M. Karlsson and B. Zietz, *J. Phys. Chem. A*, 2021, **125**, 2885–2894.
60 A. Kundu, S. Karthikeyan, Y. Sagara, D. Moon and S. P. Anthony, *ACS Omega*, 2019, **4**, 5147–5154.
61 A. L. Guzman and T. R. Hoye, *J. Org. Chem.*, 2022, **87**, 905–909.